



Parametric modeling and analysis of intake phases for side-ported Wankel rotary engines

Huaiyu Wang^b, Changwei Ji^{a,*}, Jinxin Yang^a, Yunshan Ge^b, Sergey Zambalov^c, Igor Yakovlev^c

^a College of Energy and Power Engineering, Department of Automotive Engineering, Beijing University of Technology, Beijing, 100124, PR China

^b School of Mechanical Engineering, Beijing Institute of Technology, Beijing, 100081, PR China

^c Tomsk Scientific Center, Siberian Branch, Russian Academy of Sciences, Tomsk, 634055, Russia

ARTICLE INFO

Keywords:

Wankel rotary engines
Port parametric modeling method
Intake loss
Volumetric efficiency

ABSTRACT

This research presents a novel port parametric modeling technique using three-dimensional computational fluid dynamics for the design and optimization of intake and exhaust phases in side-ported Wankel rotary engines (WREs). Definitions for the port phases encompass parameters such as port start opening, port full opening, port start closing, and port full closing timings. The four port phase control arcs are obtained by translating and rotating the rotor flank to satisfy the high control accuracy. Further, the shape of the port is further smoothed and varied by four auxiliary circular arcs. Moreover, the influence of port full closing timing and the size of auxiliary circular arcs (R1, and R3) on the intake characteristics is studied.

The results show that the novel method can flexibly and effectively control the phases and shapes. The early port full closing timing reduces fluid backflow and improves volumetric efficiency (VE) but increases intake loss (IL). The small size of R1 facilitates to increase the VE and reduce IL. A larger or smaller size of R3 is not conducive to reducing IL, and the smaller size of R3 improves the VE. The novel generation method proposed in this paper provides a theoretical basis to optimize the design of various sizes of side-ported WREs and guidance for practical manufacturing.

1. Introduction

Carbon neutrality requires reducing carbon dioxide (CO₂) emissions and transforming energy structures to achieve net-zero emissions [1,2]. To achieve long-term CO₂ emissions reduction, range extender electric vehicles (REEVs) are considered to be a favorable solution for the passenger car industry [3,4]. The REEVs offer the potential advantage of reducing fossil fuel consumption and extending battery life [5]. Given its compact design, high power-to-weight ratio, and superior NVH (noise, vibration, and harshness) attributes, scholars advocate for the adoption of the Wankel rotary engine (WRE) as a range extender [6,7]. However, its unique rotor rotation and large surface-to-volume ratio lead to low combustion efficiency, which limits its development and large-scale application [8]. Consequently, improving combustion efficiency and reducing pollutant emissions become the primary challenges for WRE development [9,10].

Given the significance of the intake structure and phases, they exert a direct influence on intake characteristics. These

* Corresponding author. College of Energy and Power Engineering, Beijing University of Technology, Beijing 100124, PR China.

E-mail addresses: nepu2017@126.com (H. Wang), chwji@bjut.edu.cn (C. Ji).

<https://doi.org/10.1016/j.heliyon.2023.e21710>

Received 4 March 2023; Received in revised form 19 October 2023; Accepted 26 October 2023

Available online 4 November 2023

2405-8440/© 2023 The Authors. Published by Elsevier Ltd. This is an open access article under the CC BY-NC-ND license (<http://creativecommons.org/licenses/by-nc-nd/4.0/>).

characteristics are integrally connected to combustion, flow field, and emissions [11]. Therefore, a proper design of intake structure is essential for WRE [12]. Turner et al. [13] observed that eliminating the intake and exhaust overlap leads to reduced emissions. In peripheral ported WREs, turbocompounding offers an optimization of power loss [14]. They also presented a two-stage compound Wankel rotary engine concept with zero overlap, which holds potential for guiding future advancements [14]. Kutlar et al. [15] modeled and studied different auxiliary ports by using a one zone WRE simulation model. The result showed that more auxiliary ports are more effective at higher rotation speeds. Ji et al. [16] and Yang et al. [17] numerical studied the compound intake method in a hydrogen-enriched WRE with hydrogen port injection and direct injection (DI). The compound intake method was concluded to effectively enhance fuel uniformity, especially at lower rotation speeds and under partial load conditions. Chen et al. [18] reached the same conclusion on the same size engine with hydrogen DI pattern. In summary, a proper phases and shapes are essential for WRE to achieve higher power and lower emissions [19].

Compared with peripheral ported WREs, the side-ported ones provide more flexibility to control the port timings and shapes [20, 21]. The side-ported configuration completely eliminated the overlap of the intake and exhaust, which increases the port area and restores the lost performance [22]. It also reduces the residual gas ratio, improves fuel consumption, and reduces hydrocarbon emissions. Numerical simulations of a WRE with side-ported [23] and peripheral-ported [24] configurations were conducted by Fan et al. The study analyzed the flow fields under various rotation speeds, intake pressures, and intake geometries. In their researches, the particle image velocimetry (PIV) was used to test the flow field in an optical side-ported WRE [23]. According to simulation findings, the RNG $k - \epsilon$ turbulence model offers a precise emulation of the flow field [24]. The PIV test results indicated vortex formation on the rotor housing central plane during the intake stroke, transitioning to a unidirectional flow in the compression stroke [23]. Their PIV result provided the basis for the calibration of the turbulence model. Taskirana et al. [25] conducted a numerical study on the influence of intake port count on flow and combustion within a side-ported WRE across varied rotational speeds. The findings indicated that in a single-side intake port configuration, both swirl and tumble motions coexisted, whereas in a dual-port setup, the opposing airflow inhibited the tumble motion.

These studies provide the theoretical basis for the design and optimization of side-ported WREs. However, for optimization problems, it is essential to build parametric models. In contrast to reciprocating piston engines, intake and exhaust phases of WREs are fixed, which is not conducive to optimization. Deng et al. [26] utilized a parametric approach to model the intake and exhaust in a peripheral ported WRE. Similarly, Wang et al. [27] applied this method to side-ported WREs. However, these studies were all conducted in one-dimensional (1-D) simulations, and no effort has been made in three-dimensional (3-D) for the side-ported WREs. Especially due to the relatively unique geometry of WRE, no parametric modeling approach can be implemented.

Addressing the existing research gap, this study introduces a straightforward, adaptable, and parametric approach for designing the shapes and phases of the side-ported WRE. Subsequently, a 3-D CFD model is developed for a parametric examination of the side-ported WRE. Following this, the methodology for generating the port phases and shapes is elaborated. Consequently, the study explores the impacts of varying intake port closing timings on the in-cylinder flow field, volumetric efficiency (VE), and intake loss (IL). Furthermore, an analysis is conducted on the influence of auxiliary arc sizes on the flow field. In summary, this research offers an innovative and pragmatic approach to the intake structure and optimization of the side-ported WRE, providing essential theoretical insights for real-world application.

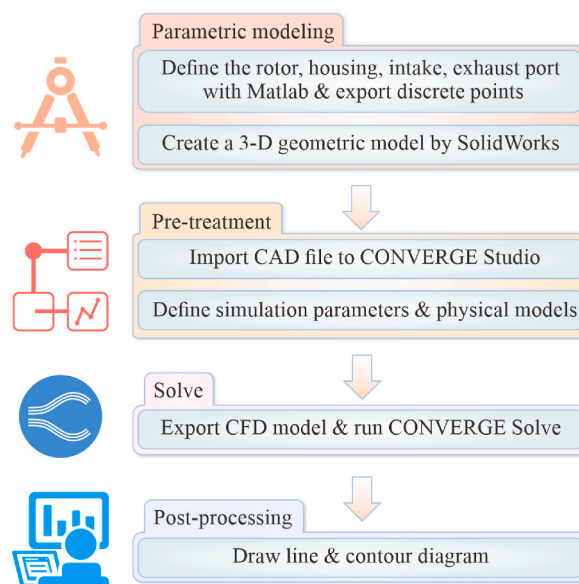


Fig. 1. Overview of the working process.

2. Simulation model construction and validation

This section focuses on modeling and validating the CFD model of the side-ported WREs. In Section 2.1, the similarities and differences between WRE and reciprocating piston engines (RPEs) are compared. Section 2.2 delineates the underlying principles and formulation methods for the housing and flank of the WRE. Following this, Section 2.3 elaborates on the 3-D CFD simulation theory along with the model configuration. A comprehensive overview of this paper’s working routine is depicted in Fig. 1.

2.1. Wankel vs. reciprocating

Fig. 2 presents a comparison of the operating principles between RPEs and WREs. Both WREs and RPEs share the commonality of having four strokes: intake, compression, expansion, and exhaust. RPEs employ a crank-link mechanism, whereas WREs utilize a planetary mechanism, leading to variations in rotation angles. For WREs, the rotation angle is defined by the eccentric angle ($^{\circ}\text{EA}$), while for RPEs, it’s determined by the crankshaft angle ($^{\circ}\text{CA}$). The complete rotation angle for WREs stands at 1080°EA , while for RPEs, it is 720°CA [28]. Fig. 3 displays the schematic of the WRE.

2.2. Wankel rotary engine principle

The geometry type of the WRE is trochoid curves, and the coordinates of the housing is formed as follows [29]:

$$\left. \begin{aligned} x &= e \cos \alpha + R \cos \frac{\alpha}{3} \\ y &= e \sin \alpha + R \sin \frac{\alpha}{3} \end{aligned} \right\} \# \tag{1}$$

In a similar manner, the coordinates of the engine rotor flank is formed as follows:

$$\left. \begin{aligned} x &= R \cos 2v + \frac{3e^2}{2R} (\cos 8v - \cos 4v) \pm e (\cos 5v + \cos v) \left(1 - \frac{9e^2}{R^2} \sin^2 3v \right)^{1/2} \\ y &= R \sin 2v + \frac{3e^2}{2R} (\sin 8v + \sin 4v) \pm e (\sin 5v - \sin v) \left(1 - \frac{9e^2}{R^2} \cos^2 3v \right)^{1/2} \end{aligned} \right\} \# \tag{2}$$

where the e , α , v , and R are the eccentricity, rotation angle, control angle, and generating radius, respectively; the geometries of the rotor can be generated by control the v in the range of $(\pi/6, \pi/2)$, $(5\pi/7, \pi/6)$, and $(3\pi/2, 11\pi/6)$. The period of the equation is 2π , and the generated curve in both ‘+’ or ‘-’ is the same. The above formula is the ideal profile. When modeling a CFD model, it is necessary to translate the profile outward for a certain distance, which is called the housing offset, usually $1 \sim 2 \text{ mm}$ [30]. Detailed modeling information can be found in Ref. [29]

This study is based on a prototype of a 0.654 L displacement naturally aspirated WRE equipped with a dual-spark plug [31]. Fig. 4

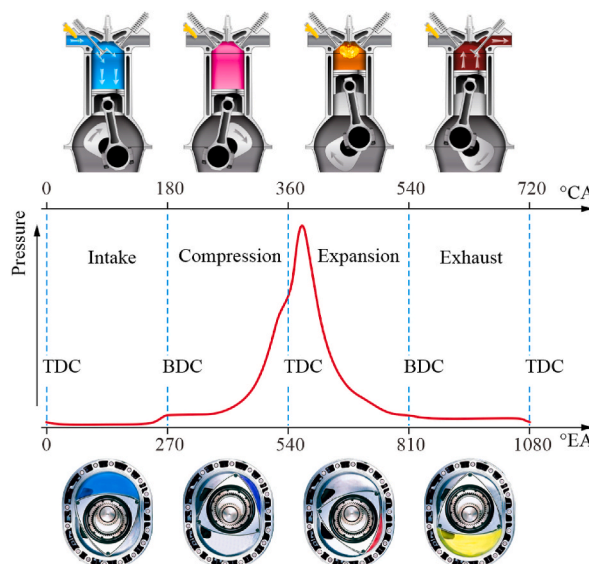


Fig. 2. Comparison of operating principles for RPEs and WREs.

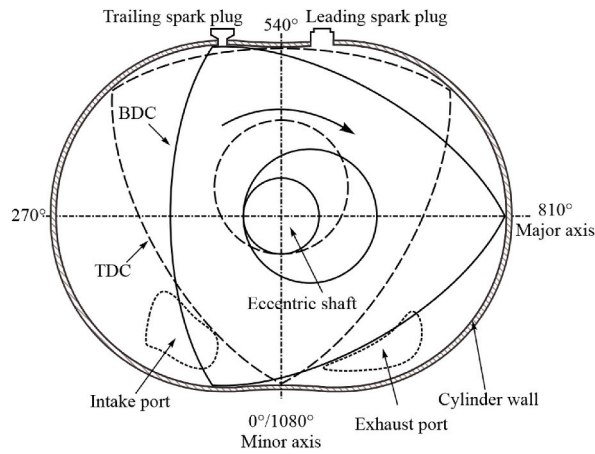


Fig. 3. Schematic of the side-ported WRE.

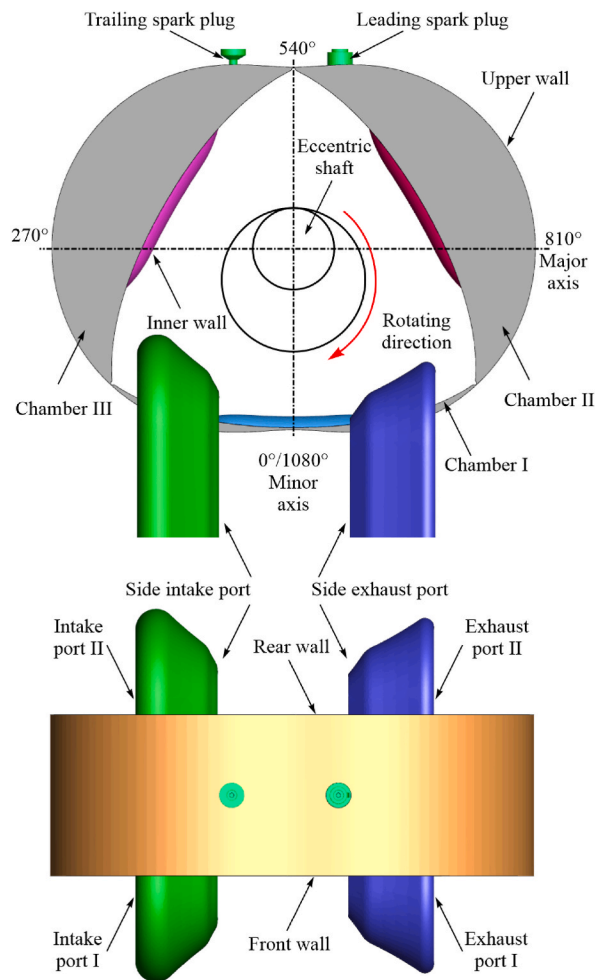


Fig. 4. Geometry of the side-ported WRE as modeled [5].

illustrates the geometry of the WRE. Table 1 details the engine’s technical specifications. The apex seal’s shape transitions from an arc to a triangle, simplifying the definition of “sealing” within CONVERGE.

2.3. Model set-up.

Table 1
Key specifications of the simulation model.

Specification	Value
Compression ratio [-]	10.0
Displacement [L]	0.654
Eccentricity [mm]	15
Generating radius [mm]	105
Width [mm]	80
Intake type	Double side port
Exhaust type	Double side port
Intake timing	3–335 °EA
Exhaust timing	760–1077 °EA

To accurately simulate the complex flow in the chamber, a suitable turbulence model is needed. Based on published experimental of PIV test [23] or numerical study [25], the RNG $k-\epsilon$ model exhibited higher prediction accuracy and capable of processing the complexity of transient turbulence and combustion phenomena [32]. The RNG $k-\epsilon$ model operates as a two-equation model: the first equation calculates the turbulent kinetic energy (k), while the second pertains to its dissipation (ϵ) [33]. The equations are presented as follows:

$$\frac{\partial \rho k}{\partial t} + \frac{\partial \rho u_i k}{\partial x_i} = \tau_{ij} \frac{\partial u_i}{\partial x_j} + \frac{\partial}{\partial x_i} \left(\frac{\mu + \mu_t}{Pr_k} \frac{\partial k}{\partial x_j} \right) - \rho \epsilon \quad (3)$$

$$\begin{aligned} \frac{\partial \rho \epsilon}{\partial t} + \frac{\partial (\rho u_i \epsilon)}{\partial x_i} = & \frac{\partial}{\partial x_j} \left(\frac{\mu + \mu_t}{Pr_\epsilon} \frac{\partial \epsilon}{\partial x_j} \right) + C_{\epsilon 3} \rho \epsilon \frac{\partial u_i}{\partial x_i} \\ & + \left(C_{\epsilon 1} \frac{\partial u_i}{\partial x_j} \tau_{ij} - C_{\epsilon 2} \rho \epsilon \right) \frac{\epsilon}{k} + S - \rho R_\epsilon \end{aligned} \quad (4)$$

In these equations, μ is velocity; ρ is density; μ_t represents turbulent viscosity; τ_{ij} is Reynolds stress; Pr_i is Prandtl number for k and ϵ equations; $C_{\epsilon i}$ are the model constants.

The objective of this study is to model and analyze the influence of the intake port shape on intake characteristics. For this purpose, the simulation adopts a higher cylinder wall temperature [34]. In fact, neither a high wall temperature nor an activated combustion model substantially impacts the simulation outcomes. Table 2 summarizes the initial and boundary conditions. Fig. 4, based on Taskiran’s findings, displays the intake and exhaust channels designed to simulate backflow [25]. Fig. 5 displays the central section of the modeled WRE, employing adaptive mesh refinement (AMR) tailored for velocity and temperature in the intake, chamber, and spark regions [35].

Grid independence verification is a crucial method to balance computational resources and model accuracy. The simulated velocity fluid with three different resolutions is plotted in Fig. 6. The legend magnitude of the velocity vectors is the same in three different resolutions. The fixed grid refinement (FGR) and AMR strategy are activated in the calculation. The base grid of three different resolutions is (a) 4.5 mm, (b) 4.0 mm, and (c) 3.5 mm. The max scale level of the AMR based on velocity and temperature is set to 2; the scale level of the FGR is set to 2, where the $scaled\ grid = base\ grid\ size / 2^n$, n is scale level. So, the minimum of the 4 mm base grid size with AMR is 1 mm, which is sufficient to simulate the WRE [23]. As illustrated in Fig. 6, the velocity fluid Fig. 6 (b) is very close to Fig. 6 (c) and better than Fig. 6 (a). Therefore, the strategy of Fig. 6 (b) is used when considering the calculation time and accuracy. The PIV test result is used to verify the turbulence model. The geometry of the tested WRE and CFD simulation model are shown in Fig. 7. Fig. 8 shows that the simulated flow field aligns well with the PIV results. Minor discrepancies in the flow field exist, attributable to the absence of a specific intake shape. However, this is within the acceptable error range in engineering and can be used for further research [25].

Table 2
Initial and boundary conditions.

Region	Value
Intake temperature [K]	300
Intake pressure [kPa]	100
Exhaust temperature [K]	700
Exhaust pressure [kPa]	100
Rotor and cylinder walls temperature [K]	550
Spark plug temperature [K]	750
Spark electrode temperature [K]	850
Operation speed [rpm]	5000
Workflow	Fresh air

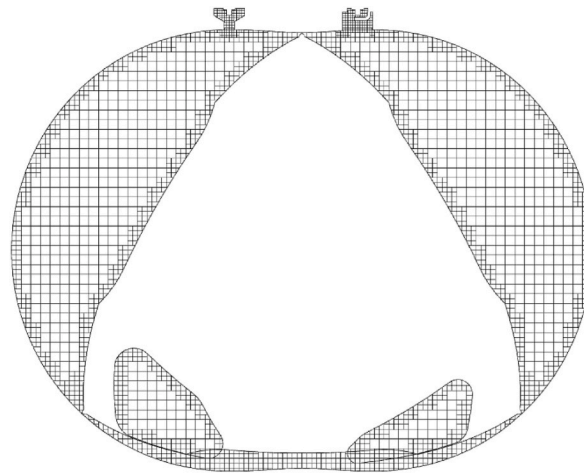


Fig. 5. Mesh of the side-ported rotary engine.

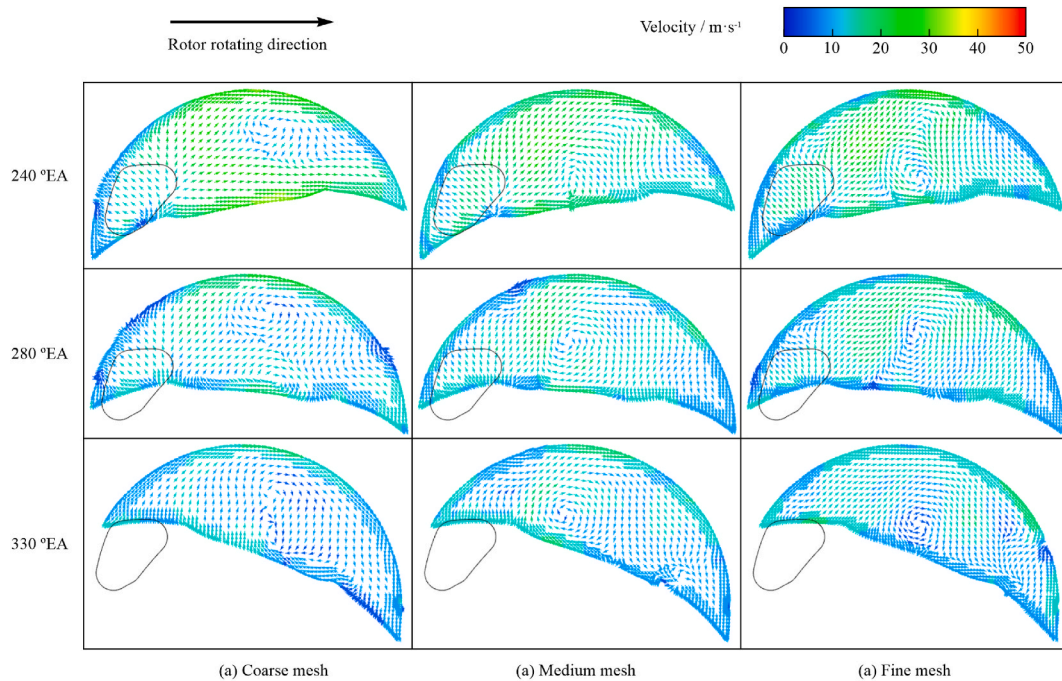


Fig. 6. Velocity profile under three different grid sizes.

3. Port shape design and research approach

3.1. Design and modeling

In order to construct a parametric model, it is essential to simplify the port phases, just like valve opening and closing [37]. Therefore, four stages are defined using trapezoids, and this simplification has been successfully applied in 1-D simulation [27]. Fig. 9 defines the process in terms of port start opening (PSO), full opening (PFO), start closing (PSC), and full closing (PFC) timings. To make the rotor flank in the corresponding phase coincide exactly with the port, the rotor flank is shifted using translation and rotation instead of simply replacing it with a circular arc. The generation method of the four port timing control arcs is shown in Fig. 10. The arcs are the intersection of the flank profile at the timing of PSO, PFO, PSC, and PFC. The gray shadow in Figs. 9 and 10 represents the real port shape. When working on a new port design, it is first necessary to enter the base parameters of the WRE, i.e., R and e. Then, the four control phases are input, i.e., PSO, PFO, PSC, and PFC. That is, this method can be used in any size of WREs. For the animation, please refer to the Supplementary Material.

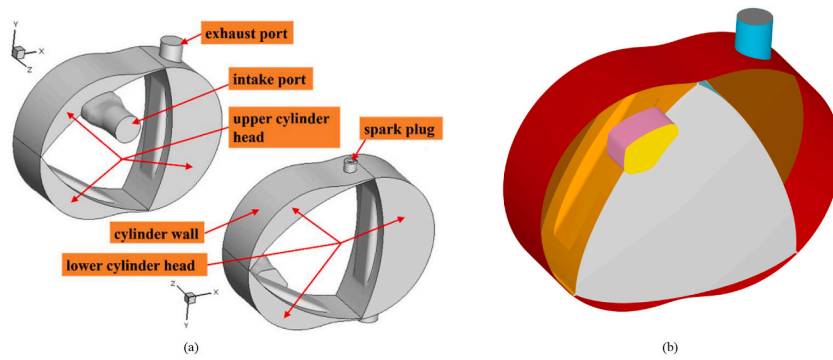


Fig. 7. The engine geometry in PIV test (a) [36] and this paper (b).

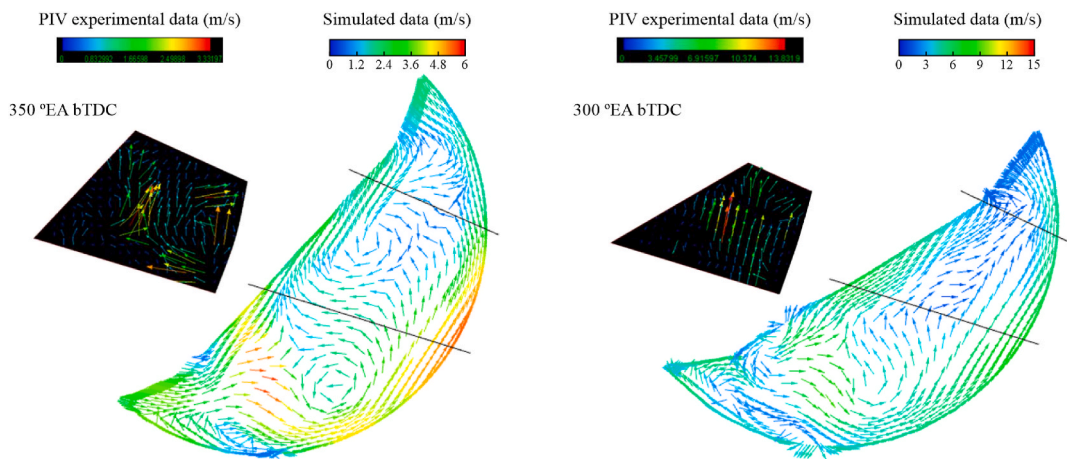


Fig. 8. Comparison of PIV experimental [36] and simulated data.

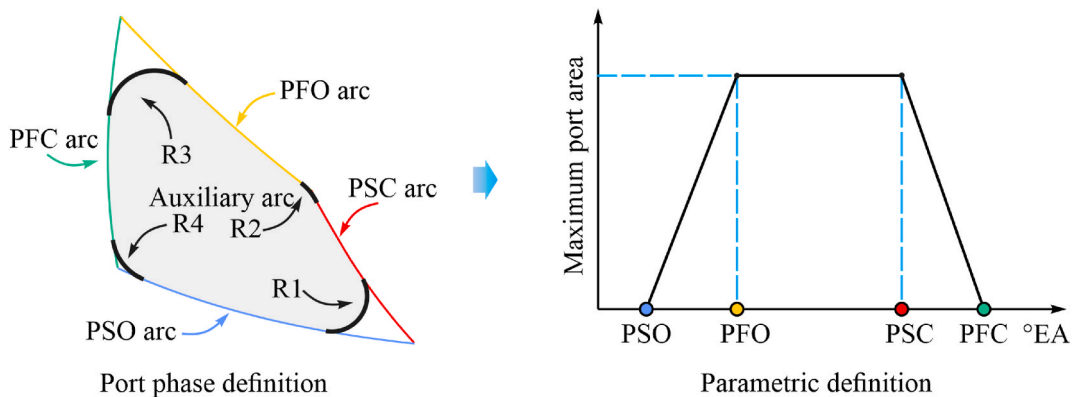


Fig. 9. Definition of port process.

The rotation method of the flank profile with various timing is shown in Fig. 11. It should be noted that the flank profile is a trochoid, not a circular arc. In this work, using a circular arc is simply than a trochoid. However, as shown in Fig. 12, it causes some clearance between rotor and port. When the rotor rotates from EA0 to EA1 timing, the flank profile first is translated to the medium point of the EA1 timing. Then, it is rotated in the same direction as the EA1 timing. The above functions can be achieved by discretizing the curve and multiplying it by the rotation matrix and translation matrix, which can be implemented in MATLAB. In addition, the auxiliary arc is to smooth the transition between the two control arcs and to facilitate machining. Since the controlled data are discrete points, it is challenging to add circular arcs, and tangency is not guaranteed, we decided to add the auxiliary arcs in the computer-aided

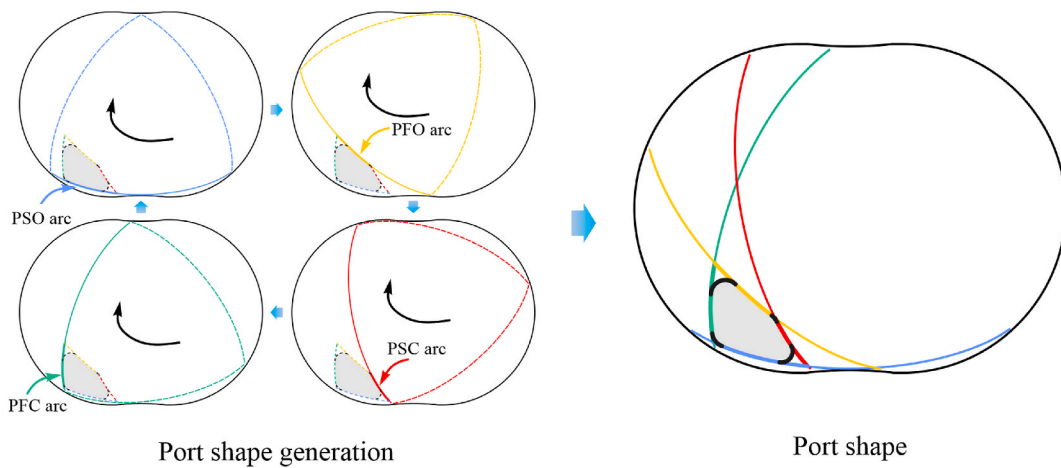


Fig. 10. Port shape generation.

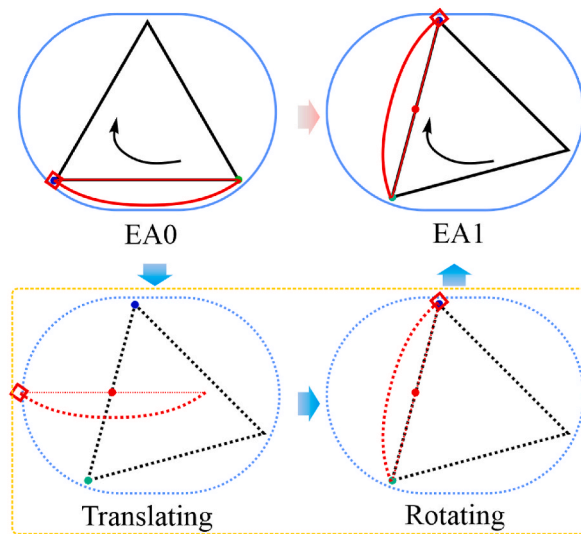


Fig. 11. Flank profile rotation method.

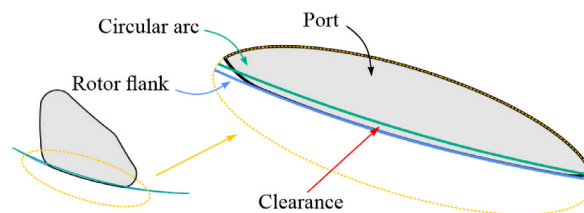


Fig. 12. Schematic diagram of clearance.

design software. However, this method needs to be tuned manually and cannot be generated automatically. It is also necessary to divide the mesh in the CONVERGE Studio for the subsequent mesh division. Future work should develop an automated process to generate computable meshes directly from a given phase. Unlike RPEs, changing the PFC timing affects the maximum area of the side-ported WREs. As presented in Fig. 13, the maximum area increases with delayed PFC timing.

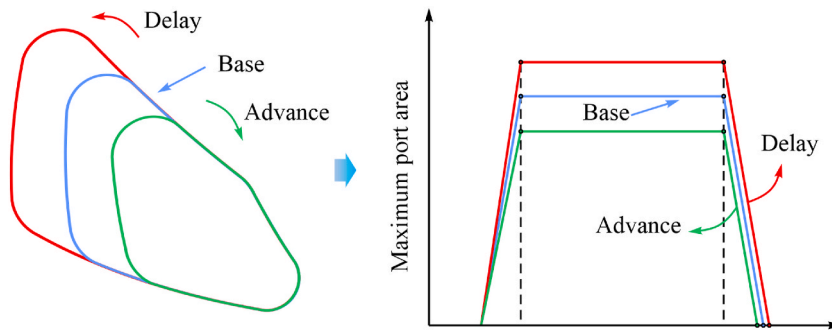


Fig. 13. Comparison of different PFC timing.

3.2. Research approach

In this section, the effect of PFC timing and auxiliary arcs of the intake port on the intake characteristics is discussed. As shown in Table 3, PFC timing change from -5 to 5°EA ; auxiliary arcs shift from "small" to "large". The diagram of the port shapes and phases is shown in Fig. 14.

4. Results and discussion

4.1. Analysis of in-cylinder pressure and flow field

In WRE, the duration of each stroke (crank angle vs. eccentric angle) is 1.5 times longer than RPEs, which facilitates adequate fuel mixing [38]. Unlike peripheral ported WRE, the side-ported ones allow for zero overlaps between intake and exhaust without sacrificing economy [13]. In addition, the intake air has no influence on the exhaust process, which contributes to the reduction of emissions [14]. To clearly and intuitively describe the geometric position, the definition of the upper, inner, front, and rear walls is presented in Fig. 4. The housing side is termed the upper wall, the recess pocket side as the inner wall, the surface linked to the side intake port I as the front, and its opposing side as the rear wall. Since the intake characteristics are similar for different phases and shapes, this section only analyzes the case 1. The pressure distribution and velocity in the combustion chamber significantly determine the IL and VE [34]. The pressure distribution and velocity in intake stroke are illustrated in Figs. 15 and 16. As shown in Fig. 15, the higher velocity of flow field is located at the middle of the chamber and the intake port. This is because the volume of the combustion chamber is smaller at this timing and the airflow can only flow through the recess. As shown in Fig. 16, the in-cylinder pressure is higher than the intake port, which causes the small backflow to the intake port. When the angle is 40°EA , the airflow of the two intake ports rushes rapidly to the chamber and collides with each other. Four small-scaled vortex cluster are formed due to the interaction of intake airflow and main flow field in the chamber. As the rotor rotates, the chamber volume continues to increase. When the angle is 80°EA , the airflow collides with the upper wall, and the two small-scaled vortex clusters form the large-scaled one. Due to the small chamber volume on the trailing side, the small-scaled vortex clusters are disappeared. At the same time, due to the impact of the airflow, the flow field slows down in the middle plane, resulting in a high-pressure zone [25]. When the rotor rotates to 120°EA , the airflow velocity slows down due to the smaller pressure difference between intake port and chamber as well as a larger chamber volume. At 200°EA , with increasing combustion chamber volume, the two airflows start to stratify, disrupting the chamber's flow field. At BDC (270°EA), the in-cylinder pressure exceeds that of the intake ports, leading to backflow. For the single side-ported WRE, a stable vortex cluster is formed in the middle of the compression stroke [23], while the dual ones do not. This is because the flow field in the dual intake results from the confrontation between the two airflows [25]. When the angle is 290°EA , the chamber is connected to the trailing spark plug and the high-pressure gas leaks from the front chamber via the trailing spark plug. This leakage may cause knock [39] in hydrogen WRE and may also lead to reduced work capacity [40]. When the angle is 320°EA , the intake stroke is coming to an end. The airflow velocity becomes faster due to the small connected area of intake port and chamber, as well as the higher in-cylinder pressure.

4.2. Analysis of intake mass flow rate

Mass flow rate affects the VE and power output. In this part, mass flow rate from two intake ports to three chambers are analyzed. In order to obtain relatively stable calculation results, each case is calculated for 3 cycles, i.e., $1080 \times 3^\circ\text{EA}$, and only the last cycle is analyzed. In fact, within the first cycle, when the chamber III intake process is finished, the intake flow has started to stabilize. Fig. 17 shows the mass flow rate for the case 1. The positive numbers represent the inflow and the negative numbers represent the outflow. As illustrated in Fig. 17 (a), the mass flow rate of the two intake ports is different. The non-uniform flow field within the cylinder leads to varying pressure disparities, consequently influencing the intake mass flow rates. It should be noted that there is a small fluctuation at the beginning of the intake stroke. As mentioned above, the higher in-cylinder pressure causes the small backflow. At the end of the intake stroke, as the cylinder volume decreases, the in-cylinder pressure increases, resulting in a backflow [25]. According to Wang

Table 3
Summary of timing and arc case setup.

Num.	Case	PFC timing (°EA)	Auxiliary R1	Auxiliary R3
1	PFC0	-	-	-
2	PFC-5	-5	-	-
3	PFC+5	+5	-	-
4	PFC0-LR1	-	↑	-
5	PFC0-SR1	-	↓	-
6	PFC0-LR3	-	-	↑
7	PFC0-SR3	-	-	↓

“-” represents the basic parameters; “↑” represents a large arc; “↓” represents a small arc.

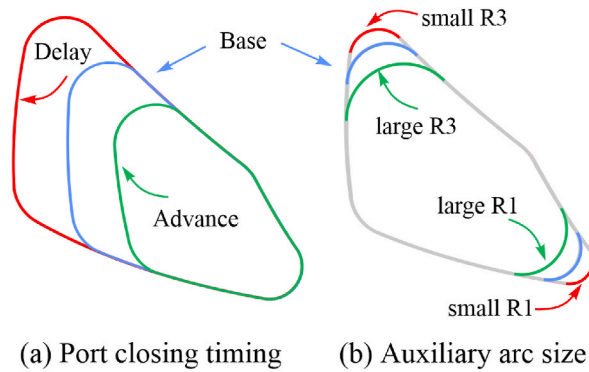


Fig. 14. The diagram of the case setup.

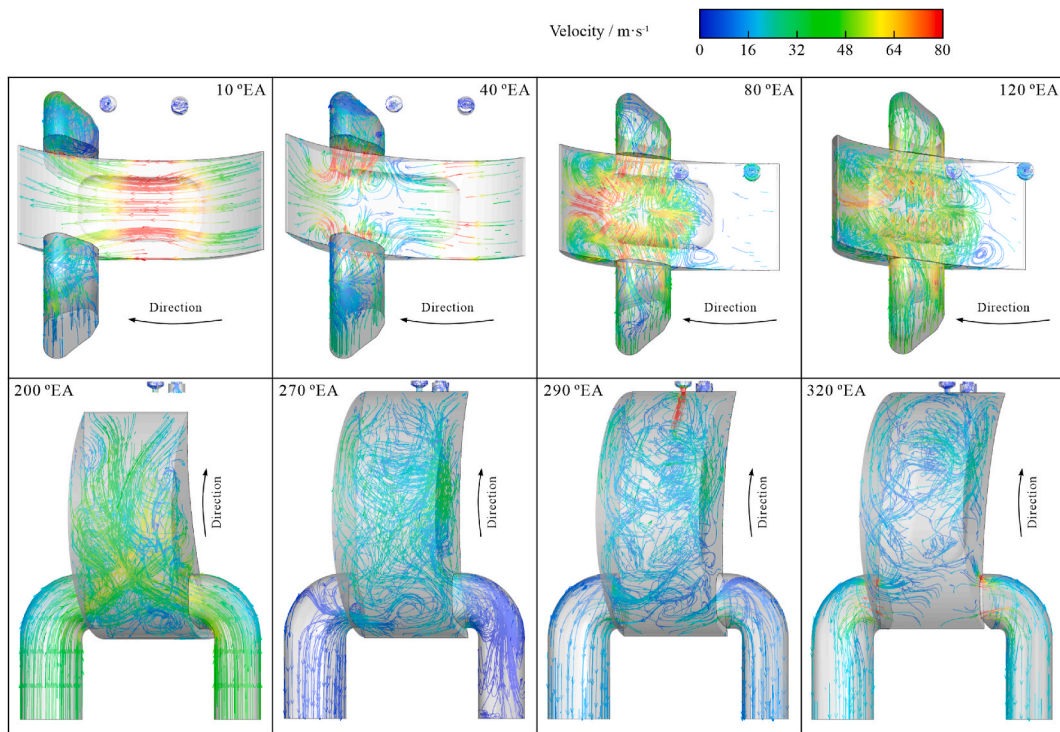


Fig. 15. Visualization of streamlines during the intake stroke.

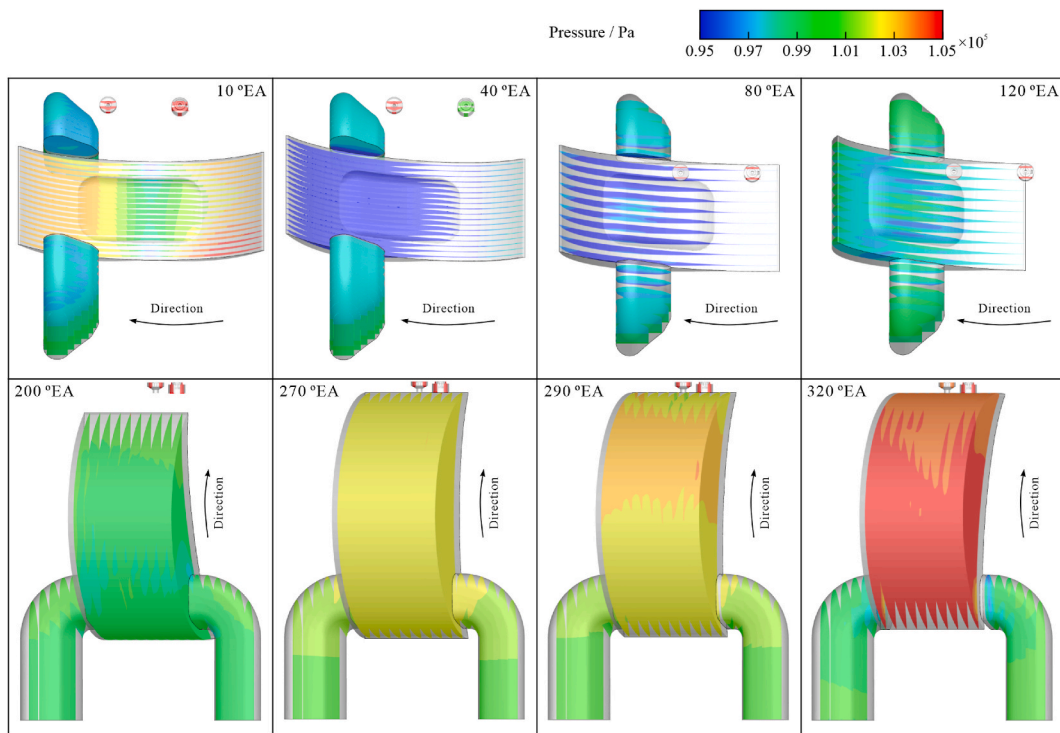


Fig. 16. Depiction of pressure distributions during the intake stroke.

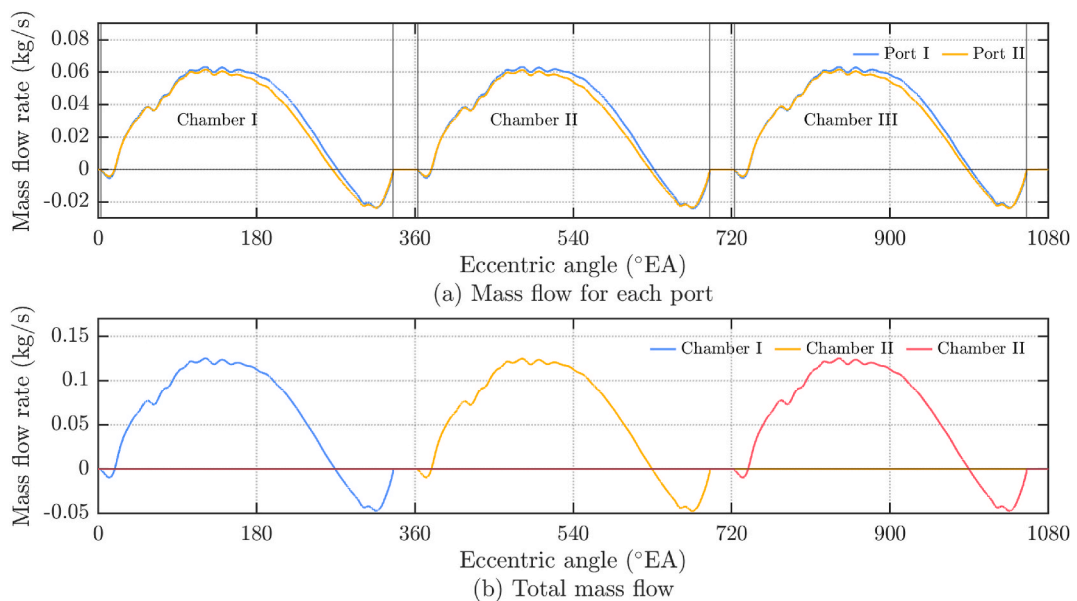


Fig. 17. Mass flow of each port and total for case 1.

et al. [40], the early PFC timing can reduce backflow, which helps to improve the engine work capacity. For RPEs, the delayed intake phases provide a Miller cycle, which improves thermal efficiency. However, for the hydrogen WRE, it is a complex problem to solve the trade-off between power and thermal efficiency [14]. As shown in Fig. 17 (b), the maximum flow rate is approximately 0.12 kg/s and the flow curve is relatively flat, which helps reduce IL. In the research [34], the total mass flow rate profile in the intake stroke is multi-peaks for an opposed rotary piston engine, whose displacement is 0.55 L, and the maximum mass flow rate is 0.135 kg/s at 3000 rpm.

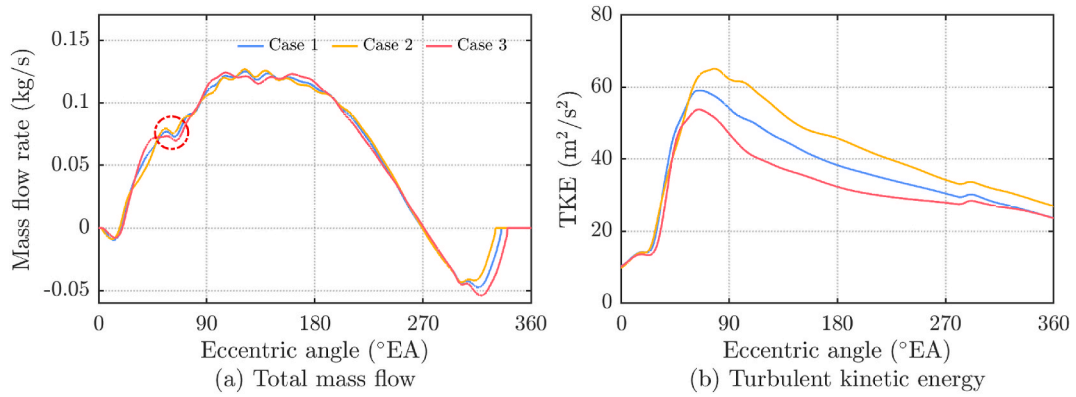


Fig. 18. Total mass flow rate and TKE comparison across various PFCs.

Fig. 18-Fig. 20 show the comparison of the total mass flow and turbulent kinetic energy (TKE) for case 1 to 7. There is a more pronounced fluctuation in Figs. 18–20 marked by red circle. This is because the high-pressure zone in the middle of the combustion chamber reduces the pressure difference between the combustion chamber and the channels. As presented in Fig. 15, the airflow collision generates the high-pressure zone [25]. As depicted in Fig. 18, case 2 exhibits a higher maximum mass flow rate compared to the others, leading to an elevated TKE [24]. At the end stage of intake stroke, the backflow of case 3 is higher than others. The above results show that the early PFC timing can increase the TKE and reduce the backflow, thus increasing the power output capacity [14]. As shown in Fig. 19, the size of R1 has a small effect on the mass flow rate, while it has a large effect on the TKE. A larger R1 results in a smaller port area and vice versa. During the initial phases of the intake stroke, the size of R1 exerts minimal influence on the intake port’s through-flow area, leading to nearly identical mass and TKE values for cases 1, 4, and 5. The effect of R1 on the through-flow area is greater at this time when the rotor rotates near 60°EA. Since the through-flow area of case 4 is smaller than that of case 1 and 5, the air flow velocity is larger, resulting in a higher TKE. As present in Fig. 20, the maximum TKE still occurs around 60°EA. The effect of R3 is the smallest, but also the most complex. At the beginning of the intake stroke, when the rotor is not rotating beyond R3, the through-flow area is almost consistent, resulting in same mass flow rates and TKE for cases 1, 6 and 7. Upon rotating beyond the PFO, the rotor achieves its maximum through-flow area. Compared to case 1 and case 7, case 6 has a smaller port area, leading to an elevated TKE. The size of R3 directly affects the maximum area of the port, and also affects the fluid backflow. Toward the conclusion of the intake process, case 7 exhibits notably greater fluid backflow compared to cases 1 and 6. This is because the fluid backflow is area-dependent, and a larger port area leads to a larger fluid backflow, which is also the same conclusion as in cases 1, 2 and 3. The above study concludes that combining PFC timing with R1 size to optimize TKE is a promising solution.

4.3. Analysis of characteristics

This paper employs IL and VE as the primary indicators for evaluating intake characteristics [34]. VE represents the ratio of actual mass to theoretical mass entering the combustion chamber, defined as follows [25].

$$\eta_v = \frac{m_a}{\rho_a V_d} \# \tag{5}$$

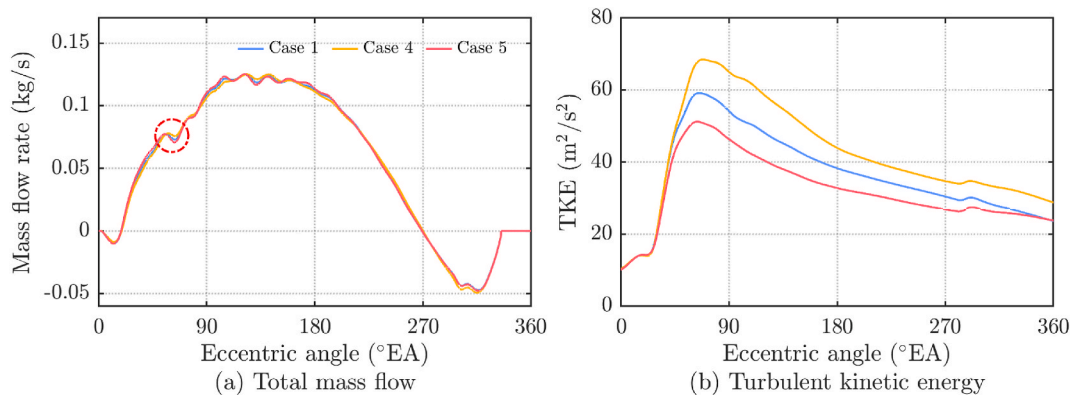


Fig. 19. Total mass flow rate and TKE across various R1 sizes.

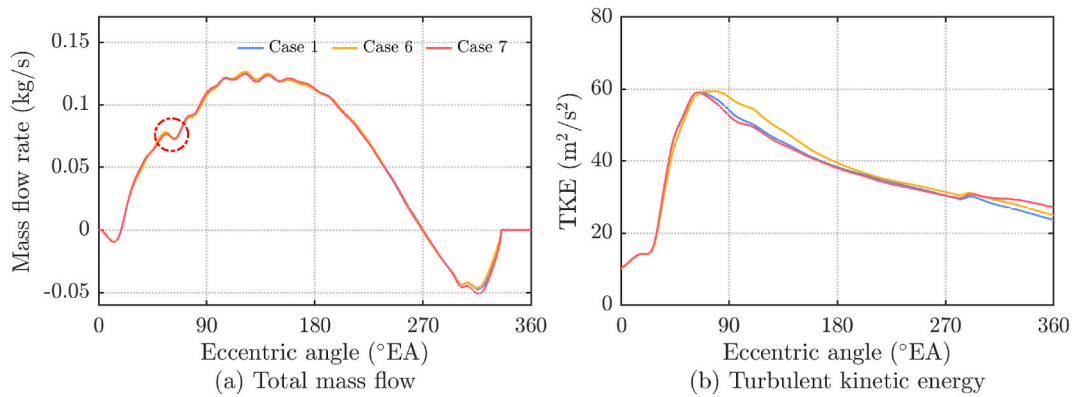


Fig. 20. Total mass flow rate and TKE across various R3 sizes.

where, the m_a is the actual mass, the ρ_a is the charge density, and the V_d is the displacement.

Given the focus on intake characteristics, the combustion model remains deactivated, with a higher wall temperature established to mitigate disturbances from the combustion process [34]. Additionally, this methodology reduces computational time. As depicted in Fig. 21, the intake air loss corresponds to the integral of the area beneath the ambient pressure line on the P–V diagram throughout the intake stroke. In numerical terms, the pump loss is the sum of the intake and exhaust losses. Fig. 21 show the P–V diagram of chamber I for case 1. As depicted in Fig. 21 (b), the P–V diagram reveals distinct compression and expansion profiles, with the former elevated above the latter. This is because, during the compression stroke, the temperature in the chamber rises rapidly above the cylinder wall, resulting in heat loss from the chamber. Another reason is that in the early stage of expansion stroke, the chamber temperature is still higher than the wall, which causes the heat transfer loss.

The intake characteristics are depicted in Fig. 22 and detailed in Table 4. Referring to Fig. 22, it can be observed that the influences on intake characteristics rank in the order of PFC timing, followed by R1 size, and then R3 size. Fig. 23–Fig. 25 present the corresponding P–V diagram below the ambient pressure line and in-cylinder mass, where the in-cylinder mass is the more visual way to demonstrate VE. As shown in Fig. 23, the trough of the P–V curve increases with advancement of the PFC timing. When at a larger volume, the P–V curve of case 2 is lower than others, which causes a higher IL [40]. Consequently, a trade-off exists between IL and VE. The PFC timing should be optimized to enhance the suitability of RE for future applications. For the influence of R1 size, as shown in Fig. 24, the P–V curve and in-cylinder mass of case 4 are lower than others, which results a higher IL and lower VE. It can be concluded that smaller R1 can achieve better performance. It is more complex for the influence of R3 size the intake characteristic. One is that the R3 size affects the maximum intake port area, which directly affects the intake characteristics, and the other is that R3 affects the intake backflow. As illustrated in Fig. 25, when the volume is less than 0.2 L, the P–V curve is almost the same. The case 6 and 7 fluctuate on both sides of case 1 when it is greater than 0.2 L and the intersection point is about 0.3 L. The intake port area of case 6 is less than others, which leads a higher VE.

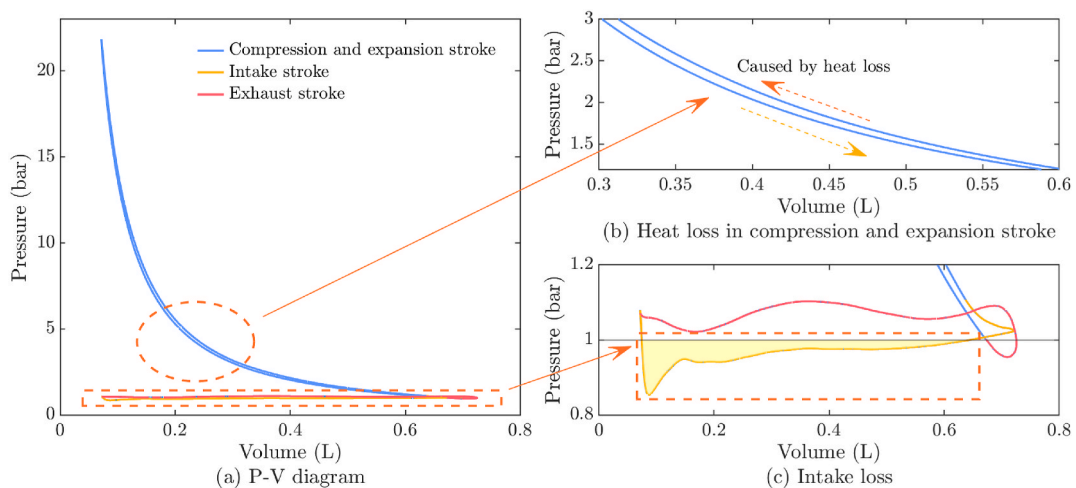


Fig. 21. Illustration of intake loss on the P–V diagram.

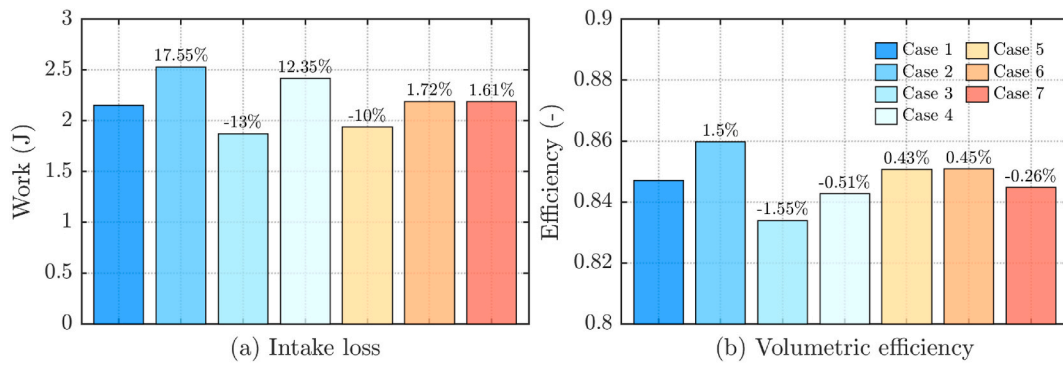


Fig. 22. Assessment of intake characteristics for various parameters.

Table 4
Detailed parameters for different configurations.

Num.	Case	IL (J)	VE (-)
1	PFC0	2.1518	0.8470
2	PFC-5	2.5294	0.8597
3	PFC+5	1.8720	0.8339
4	PFC0-LR1	2.4175	0.8427
5	PFC0-SR1	1.9366	0.8507
6	PFC0-LR3	2.1888	0.8508
7	PFC0-SR3	2.1863	0.8448

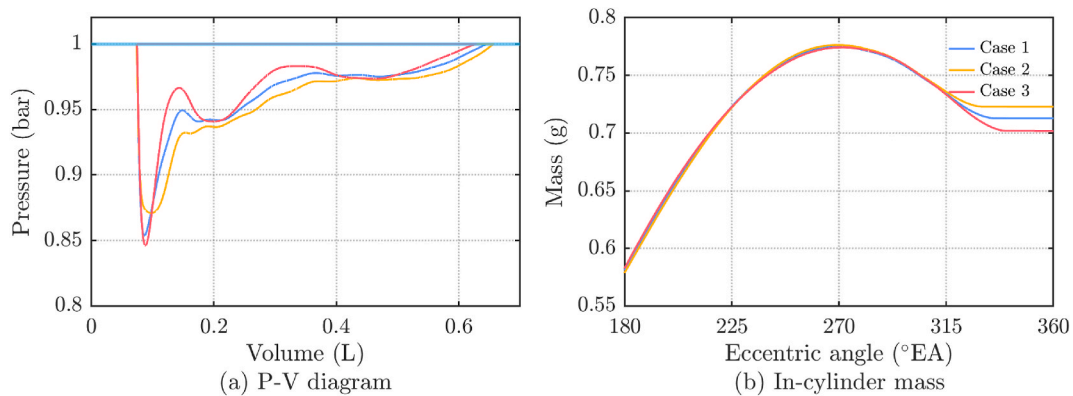


Fig. 23. P-V diagram and in-cylinder mass variations for varying PFC timings.

5. Conclusions

In this study, a novel parametric method is developed to free modeling and control the port phases and shapes of the side-ported WREs. The effects of intake phase and shape on IL and VE are analyzed. The principal investigation findings are as follows.

- 1) The developed port phases and shapes generation method can be used for various sizes of WRE. The four port phase control arcs generated by translating and rotating the rotor flank can be parametrically controlled by port phases. The smooth port shape curve is constructed by coupling four auxiliary arcs with the four port phase control arcs. Compared with circular arc, the curve generated by this method can accurately control the port phase and fit the rotor flank profile.
- 2) For the double side intake ported WRE, when the rotor rotates to 40°EA, the stable symmetrical vortex clusters are formed on the leading side of the combustion chamber. A high-pressure zone is formed in the middle of the combustion chamber. As the combustion chamber volume increases, two airflow streams from different intake ports start to stratify, and the main flow field is disturbed. When the chamber moves to the maximum volume, the backflow occurs due to the higher in-cylinder pressure.
- 3) Seven distinct phases and shapes have been formulated using this method, and their intake characteristics have been evaluated. Relative to the sizes of R1 and R3, it is the PFC timing that predominantly influences the intake characteristics which results in a trade-off between IL and VE. A reduced size of the R1 auxiliary arc enhances volumetric efficiency while diminishing IL. The size of

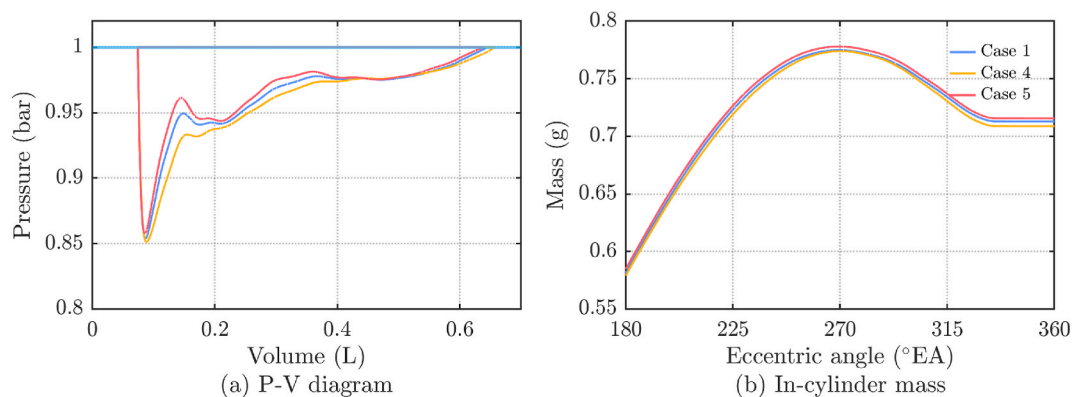


Fig. 24. P-V diagram and in-cylinder mass variations for varying R1 sizes.

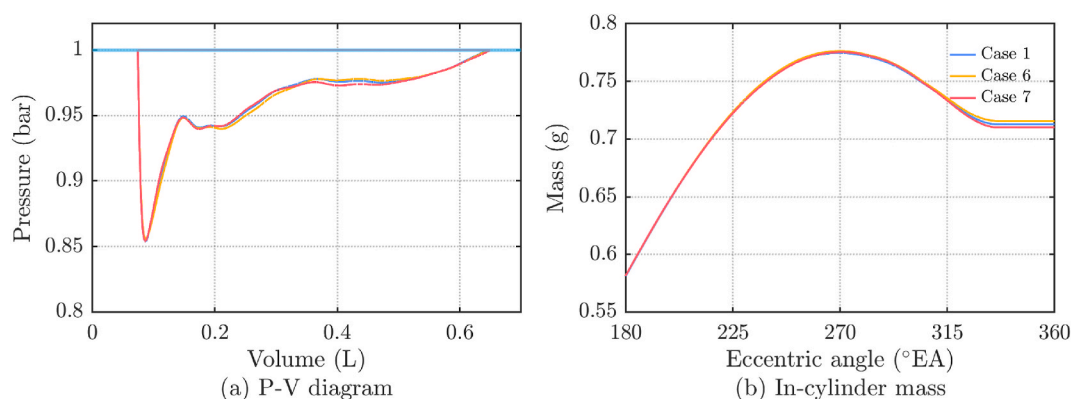


Fig. 25. P-V diagram and in-cylinder mass variations for varying R3 sizes.

the R3 auxiliary arc exerts a multifaceted impact on the intake characteristics. Optimal port design facilitates the concurrent enhancement of VE and mitigation of IL.

The limitations and inspiration are as follows.

- 1) This study developed a parametric modeling approach, but it requires manual adjustment and partitioning of the mesh, and future research efforts should focus on automating the process. The development of automated mesh processing using Python might be a worthwhile approach to investigate.
- 2) The developed parametric model solved the basic part of the optimization process, and future work should be done in two areas: one is to develop machine learning models to predict IL and VE; the other is to combine 1-D simulation for fast optimization.

This research signifies a crucial progression in the quest for efficient and eco-friendly WREs. Moreover, it lays the groundwork for refining the design of the WRE intake system, which is poised to be a primary emphasis in future research endeavors.

Data availability statement

The authors do not have permission to share data.

CRediT authorship contribution statement

Huaiyu Wang: Conceptualization, Formal analysis, Software, Validation, Visualization, Writing – original draft, Writing – review & editing. **Changwei Ji:** Funding acquisition, Investigation, Project administration, Writing – review & editing. **Jinxin Yang:** Conceptualization, Investigation, Methodology, Software, Supervision, Writing – review & editing. **Yunshan Ge:** Data curation, Investigation, Supervision, Writing – review & editing. **Sergey Zambalov:** Funding acquisition, Methodology, Software, Validation, Writing – review & editing. **Igor Yakovlev:** Data curation, Methodology, Supervision, Writing – review & editing.

Declaration of competing interest

The authors declare that they have no known competing financial interests or personal relationships that could have appeared to influence the work reported in this paper.

Acknowledgements

This work was supported by the National Natural Science Foundation of China (NO.51976003), the Ministry of Science and Higher Education, Russian Federation, public contract of Tomsk Scientific Center, Siberian Branch, Russian Academy of Sciences, and the BIT Research and Innovation Promoting Project (Grant No.2022YCXZ004).

Appendix B. Supplementary data

Supplementary data to this article can be found online at <https://doi.org/10.1016/j.heliyon.2023.e21710>.

References

- [1] X. Duan, L. Feng, H. Liu, et al., Experimental investigation on exhaust emissions of a heavy-duty vehicle powered by a methanol-fuelled spark ignition engine under world Harmonized Transient Cycle and actual on-road driving conditions, *Energy* 282 (2023), 128869.
- [2] L. Xu, Z. Yang, J. Chen, et al., Impacts of the COVID-19 epidemic on carbon emissions from international shipping, *Mar. Pollut. Bull.* 189 (2023), 114730.
- [3] Y. Wang, H. Zhao, H. Yin, et al., Quantitative study of vehicle CO₂ emission at various temperatures and road loads, *Fuel* 320 (2022), 123911.
- [4] C. Shi, S. Chai, L. Di, et al., Combined experimental-numerical analysis of hydrogen as a combustion enhancer applied to wankel engine, *Energy* 263 (2023), 125896.
- [5] S. Zambalov, I. Yakovlev, A. Maznoy, Effect of multiple fuel injection strategies on mixture formation and combustion in a hydrogen-fueled rotary range extender for battery electric vehicles, *Energy Convers. Manag.* 220 (2020), 113097.
- [6] C. Shi, S. Chai, H. Wang, et al., An insight into direct water injection applied on the hydrogen-enriched rotary engine, *Fuel* 339 (2023), 127352.
- [7] H. Meng, C. Ji, S. Wang, et al., A review: centurial progress and development of Wankel rotary engine, *Fuel* 335 (2023), 127043.
- [8] J. Turner, R. Islam, G. Vorraro, et al., Investigations into steady-state and stop-start emissions in a Wankel rotary engine with a novel rotor cooling arrangement, *SAE Technical Paper* (2021), 2021-24-0097.
- [9] H. Wang, C. Ji, C. Shi, et al., Comparison and evaluation of advanced machine learning methods for performance and emissions prediction of a gasoline Wankel rotary engine, *Energy* 248 (2022), 123611.
- [10] O.A. Kutlar, F. Malkaz, Two-stroke Wankel type rotary engine: a new approach for higher power density, *Energies* 12 (21) (2019) 4096.
- [11] C. Hsieh, K. Chen, T. Johar, Fluid flow characteristics of two types rotary engines, *Int. J. Hydrogen Energy* 46 (80) (2021) 40154–40174.
- [12] D. Jeng, M. Hsieh, C. Lee, et al., The Intake and Exhaust Pipe Effect on Rotary Engine Performance, *SAE Technical Paper*, 2013, 2013-32-9161.
- [13] J. Turner, M. Turner, G. Vorraro, et al., Initial investigations into the benefits and challenges of eliminating port overlap in Wankel rotary engines, *SAE International Journal of Advances and Current Practices in Mobility* 2 (4) (2020) 1800–1817.
- [14] J. Turner, M. Turner, R. Islam, et al., Further Investigations into the Benefits and Challenges of Eliminating Port Overlap in Wankel Rotary Engines, *SAE Technical Paper*, 2021, 2021-01-0638.
- [15] O.A. Kutlar, Ö. Cihan, Investigation of parameters affecting rotary engine by means of a one zone thermodynamic model, *J. Energy Resour. Technol.* 144 (4) (2021).
- [16] C. Ji, H. Meng, S. Wang, et al., Realizing stratified mixtures distribution in a hydrogen-enriched gasoline Wankel engine by different compound intake methods, *Energy Convers. Manag.* 203 (2020), 112230.
- [17] J. Yang, C. Ji, S. Wang, et al., Numerical study of compound intake on mixture formation and combustion process in a hydrogen-enriched gasoline Wankel rotary engine, *Energy Convers. Manag.* 185 (2019) 66–74.
- [18] W. Chen, S. Yu, Q. Zuo, et al., Combined effect of air intake method and hydrogen injection timing on airflow movement and mixture formation in a hydrogen direct injection rotary engine, *Int. J. Hydrogen Energy* 47 (25) (2022) 12739–12758.
- [19] H. Wang, C. Ji, C. Shi, et al., Multi-objective optimization of a hydrogen-fueled Wankel rotary engine based on machine learning and genetic algorithm, *Energy* 263 (2023), 125961.
- [20] H. Wang, C. Ji, J. Yang, et al., Implementation of a novel dual-layer machine learning structure for predicting the intake characteristics of a side-ported Wankel rotary engine, *Aero. Sci. Technol.* 132 (2023), 108042.
- [21] H. Wang, C. Ji, J. Yang, et al., Towards a comprehensive optimization of the intake characteristics for side ported Wankel rotary engines by coupling machine learning with genetic algorithm, *Energy* 261 (2022), 125334.
- [22] M. Ohkubo, S. Tashima, R. Shimizu, et al., Developed Technologies of the New Rotary Engine (RENESES), *SAE Technical Paper*, 2004, 2004-01-1790.
- [23] B. Fan, J. Pan, A. Tang, et al., Experimental and numerical investigation of the fluid flow in a side-ported rotary engine, *Energy Convers. Manag.* 95 (2015) 385–397.
- [24] B. Fan, J. Pan, W. Yang, et al., Effects of different parameters on the flow field of peripheral ported rotary engines, *Engineering Applications of Computational Fluid Mechanics* 9 (1) (2015) 445–457.
- [25] O. Taskiran, A. Calik, O. Kutlar, Comparison of flow field and combustion in single and double side ported rotary engine, *Fuel* 254 (2019), 115651.
- [26] X. Deng, X. Lin, D. Jia, et al., Optimization of fully variable valve system in a diesel rotary engine, *Trans. Chin. Soc. Agric. Eng.* 37 (4) (2021) 114–121.
- [27] H. Wang, C. Ji, C. Shi, et al., Parametric modeling and optimization of the intake and exhaust phases of a hydrogen Wankel rotary engine using parallel computing optimization platform, *Fuel* 324 (2022), 124381.
- [28] H. Meng, C. Ji, G. Xin, et al., Comparison of combustion, emission and abnormal combustion of hydrogen-fueled Wankel rotary engine and reciprocating piston engine, *Fuel* 318 (2022), 123675.
- [29] M. Peden, M. Turner, J.W.G. Turner, et al., Comparison of 1-D Modelling Approaches for Wankel Engine Performance Simulation and Initial Study of the Direct Injection Limitations, *SAE Technical Paper*, 2018, 2018-01-1452.
- [30] H. Jiao, R. Zou, N. Wang, et al., Optimization design of the ignition system for Wankel rotary engine considering ignition environment, flow, and combustion, *Appl. Therm. Eng.* 201 (2022), 117713.
- [31] J. Yang, H. Meng, C. Ji, et al., Comparatively investigating the leading and trailing spark plug on the hydrogen rotary engine, *Fuel* 308 (2022), 122005.
- [32] J. Bao, P. Qu, H. Wang, et al., Implementation of various bowl designs in an HPDI natural gas engine focused on performance and pollutant emissions, *Chemosphere* 303 (2022), 135275.
- [33] K.J. Richards, P.K. Senecal, E. Pomraning, *CONVERGE 3.0 Manual*, Convergent Science, Madison, WI, 2020.

- [34] J. Gao, G. Tian, P. Jenner, et al., Intake characteristics and pumping loss in the intake stroke of a novel small scale opposed rotary piston engine, *J. Clean. Prod.* 261 (2020), 121180.
- [35] H. Wang, C. Ji, D. Wang, et al., Investigation on the potential of using carbon-free ammonia and hydrogen in small-scaled Wankel rotary engines, *Energy* 283 (2023), 129166.
- [36] B. Fan, Y. Zhang, J. Pan, et al., Experimental and numerical study on the formation mechanism of flow field in a side-ported rotary engine considering apex seal leakage, *J. Energy Resour. Technol.* 143 (2) (2020).
- [37] C. Ji, C. Hong, S. Wang, et al., Evaluation of the variable valve timing strategy in a direct-injection hydrogen engine with the Miller cycle under lean conditions, *Fuel* 343 (2023), 127932.
- [38] J. Bao, H. Wang, R. Wang, et al., Comparative experimental study on macroscopic spray characteristics of various oxygenated diesel fuels, *Energy Sci. Eng.* 11 (5) (2023) 1579–1588.
- [39] H. Meng, C. Ji, T. Su, et al., Analyzing characteristics of knock in a hydrogen-fueled Wankel rotary engine, *Energy* 250 (2022), 123828.
- [40] H. Wang, C. Ji, C. Shi, et al., Modeling and parametric study of the performance-emissions trade-off of a hydrogen Wankel rotary engine, *Fuel* 318 (2022), 123662.